ACCSCIENCE PUBLISHING

International Journal of Bioprinting

ACCEPTED PAPER · MAIN TEXT

Data-driven rheology enables predictive embedded bioprinting

Article ID: IJB026200187

Citation: Wang J, Zhang W, Yang K, Zheng B, Li Q. Data-driven rheology enables predictive embedded bioprinting. *Int J Bioprint.* 2026. doi: 10.36922/IJB026200187

AccScience Publishing
RESEARCH ARTICLE
Volume X Issue X (2026)
doi: 10.36922/IJB026200187

Data-driven rheology enables predictive embedded bioprinting

Running title: Data-driven precise bioprinting

Junyan Wang, Wenzhen Zhang, Ke Yang, Bowen Zheng, and Qi Li*

School of Engineering, Hangzhou Normal University, Hangzhou, 311121, China

(This article belongs to the *Special Issue: Intelligent bioprinting: From printable structures to functional systems*)

***Corresponding author:**
Qi Li (lqhznu@hznu.edu.cn)

Citation: Wang J, Zhang W, Yang K, Zheng B, Li Q. Data-driven rheology enables predictive embedded bioprinting. *Int J Bioprint.* 2026. doi: 10.36922/IJB026200187

Received: May 13, 2026
Revised: June 12, 2026
Accepted: June 16, 2026
Published online: June 16, 2026

Abstract

Precise control of filament formation remains a central barrier in extrusion-based bioprinting, where small deviations in material behavior can lead to large variations in structure and cellular outcome. Here, we present a data-driven rheology framework that enables predictive embedded bioprinting by directly linking material behavior to process outcome. A machine learning (ML) model was used to capture the coupled temperature-shear response of a thermosensitive GelMA bioink and the shear-dependent behavior of the supporting bath, and was integrated into process analysis. This approach improved the prediction of both flow disturbance and filament geometry, with reduced errors in aspect ratio and filament width compared to conventional constitutive models. The improved predictability translated into controllable fabrication, enabling stable filament formation across a wide size range (≈160-800 μm) and the reliable construction of ultra-soft, freeform, and overhanging structures with preserved three-dimensional fidelity. This level of control also carried biological consequences, as well-defined filaments supported faster post-printing recovery, enhanced alignment, stronger MHC expression, and transcriptional signatures consistent with a more favorable differentiation state. These results show that improving rheological description could move embedded bioprinting toward predictive manufacturing, where geometry and biological outcome can be coordinated through material-informed design.

Keywords: Biofabrication; Bioprinting; Embedded bioprinting; Printability

1. Introduction

Engineering functional tissues requires control over more than bulk shape[1,2]. In many native systems, including skeletal muscle[3], blood vessels[4], and other organized tissues[5], biological performance emerges from well-defined microarchitecture, where local geometry governs cell alignment, extracellular matrix organization, mass transport, and tissue maturation[6,7]. Precise biofabrication is therefore central to tissue engineering, particularly when the goal is to reproduce not only anatomical form but also structure-guided function.

Extrusion-based bioprinting is one of the most widely used biofabrication strategies because of its accessibility, versatility, and compatibility with a broad range of biomaterials and cell types[8-10]. Embedded bioprinting further expands this capability by depositing soft bioinks within a supporting bath, enabling the fabrication of freeform, highly compliant, and overhanging structures that would otherwise collapse during printing[11]. This feature makes embedded printing especially attractive for constructing biomimetic tissues with complex geometries[12,13]. Even so, achieving true printing precision in these systems remains difficult[14,15]. Filament width, cross-sectional shape, continuity, and local bath disturbance are highly sensitive to processing conditions, and relatively small variations can lead to major differences in the final construct.

Considerable efforts have been made to model extrusion and deposition in order to improve printing predictability. These studies have advanced the understanding of nozzle flow, filament spreading, and supporting bath interaction, yet accurate prediction of printing outcomes remains challenging, especially in embedded systems using thermosensitive bioinks[16,17]. A major limitation of current approaches lies in the simplified treatment of rheology[18]. Many temperature-sensitive bioinks and polymeric hydrogels exhibit rheological properties governed by temperature-dependent microstructural evolution. In materials such as GelMA, temperature can alter chain entanglement, physical crosslinking, and partial triple-helix formation, thereby affecting both viscosity and shear response. Conventional Power-Law models (PL) neglect temperature effects, while temperature-dependent constitutive models typically incorporate temperature through empirical parameter corrections. However, these

approaches generally assume that temperature and shear-rate effects are independent, with temperature acting only to modify model parameters rather than the underlying flow mechanism. Consequently, they often struggle to capture the coupled and nonlinear temperature-shear behavior of thermosensitive bioinks (Figure S1). During printing, the bioink experiences changing thermal conditions from the syringe to the nozzle and then into the supporting bath[19]. Under these conditions, viscosity is not controlled by shear alone, but by the coupled influence of temperature and shear rate. Ignoring this coupling introduces systematic errors in estimating flow behavior and ultimately limits the prediction of filament diameter, stability, and bath disturbance[20].

To address these challenges, we developed a data-driven rheology framework for predictive embedded bioprinting. A machine learning model (ML model) was used to describe the coupled temperature-shear behavior of a thermosensitive GelMA bioink and the shear-dependent rheology of the supporting bath. These rheological models were incorporated into process analysis to predict supporting bath disturbance and filament formation under different printing conditions. The framework improved the prediction of flow disturbance and filament geometry relative to conventional constitutive models, enabled the definition of a stable printing window, and supported the fabrication of precise freeform structures. We further show that well-defined filaments promote faster early recovery, stronger myogenic organization, and transcriptomic changes associated with a more favorable maturation state (Figure 1). Together, these results show how improved rheological prediction can support precise and biologically meaningful embedded bioprinting.

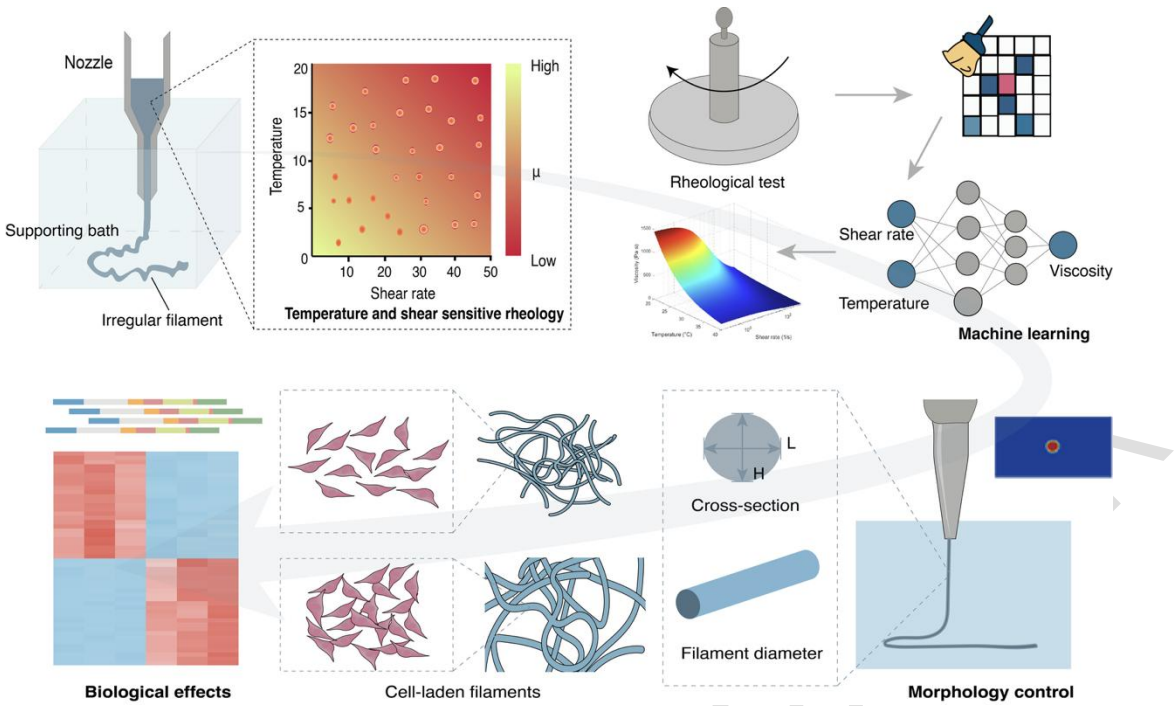

Figure 1. Schematic illustration of the overall workflow. Rheological measurements were performed to capture the coupled effects of temperature and shear rate on bioink behavior and the shear-dependent response of the supporting bath. A ML-based rheology model was then trained and incorporated into numerical simulations to predict supporting bath disturbance and filament formation under different printing conditions. The resulting predictive framework was further used to define printable regimes, guide geometry programming, and evaluate how filament architecture influences downstream cellular organization and maturation.

2. Materials and methods

2.1. Preparation of supporting bath, bioink, and removal solution

The supporting matrix was formulated using a combination of hydroxypropyl methylcellulose (H-HPMC, 3% w/v; Sangelose 90L, Daido Chemical, Japan) and Pluronic F127 (PF-127, 10% w/v; Sigma-Aldrich, USA). This specific combination was validated in our previous study to provide an optimal viscoelastic network via hydrophobic association. The network is characterized by a well-defined yield stress of ~10.3 Pa and a short characteristic recovery time upon shear cessation, which collectively ensure high printing fidelity and stable rheological

properties within the temperature window of 22℃ to 30℃[21]. PF-127 powder was first dissolved in phosphate-buffered saline (PBS, Biosharp, China) at 4℃ overnight to ensure complete solubilization. The solution was subsequently heated to 50℃ under continuous stirring, followed by gradual incorporation of H-HPMC at 750 rpm. The mixture was then cooled to room temperature (25℃) while maintaining agitation and transferred into a transparent acrylic container for subsequent printing experiments.

Gelatin methacryloyl (GelMA, EFL, China) was used as the bioink matrix, including a conventional formulation (EFL-GM-60, 60% substitution, lyophilized as a white spongy solid) and a porous formulation (EFL-GM-PR-001), which forms interconnected pores (tens to hundreds of micrometers) upon photocrosslinking and consists of GelMA (60% substitution), polyethylene oxide (Mw 300 kDa), and LAP in a 100:15:5 ratio. GelMA is a widely used bioink in tissue engineering due to its excellent biocompatibility, tunable mechanical properties, and rapid photocrosslinking capability. However, its pronounced temperature-dependent rheological behavior within the printing-relevant temperature range makes it intrinsically difficult to print with consistent quality. Precisely because of this challenging thermosensitivity, GelMA serves as an ideal benchmark material for evaluating the proposed temperature-coupled rheological framework. To facilitate visualization, 0.1% (w/v) food dye was incorporated.

A 5% (v/v) polyethylene glycol 400 (PEG400, SCR, China) solution in PBS was prepared as the removal bath.

All materials and solutions were sterilized prior to use. PF-127, GelMA, and PEG400 solutions were filtered through 0.22 μm membranes, while H-HPMC powder was sterilized by UV exposure for 30 min. All devices in contact with cell-laden materials were UV-sterilized to minimize contamination.

2.2. Rheological characterization

Rheological properties of the bioink and the supporting bath were evaluated using a rotational rheometer (Discovery Core Rheometer, TA Instruments, USA) equipped with a 40 mm parallel

plate geometry and a 1 mm gap. Shear-thinning behavior was assessed through shear rate sweeps (0.001-100 s^{-1}, logarithmic scale) over a temperature range of 20-30℃ with 1℃ increments (Figure S2). The acquired data were fitted with the Herschel-Bulkley model (HB) and power law model, which is expressed as follows

$$\sigma = \sigma_y + k\dot{\gamma}^n, \quad \text{(I)}$$

$$\mu = k\dot{\gamma}^{n-1}, \quad \text{(II)}$$

where σ is the shear stress, σ_y is the yield stress, $\dot{\gamma}$ is the shear rate, μ is the viscosity, k is the flow consistency index, and n is the flow behavior index.

2.3. PIV analysis of flow field

To visualize flow dynamics within the supporting bath, fluorescent tracer particles (2 μm diameter, excitation at 527 nm; Beiting, China) were dispersed at a concentration of 1×10^7 particles mL^{-1}. The suspension was loaded into a transparent cubic chamber (30 × 30 × 30 mm), which was mounted on a linear translation stage to simulate nozzle movement. Flow visualization was recorded using a camera (MV-SUA133GM, MindVision, China) positioned beneath the setup. A series of experiments was conducted using nozzles of identical length (38 mm) but varying diameters. Translation speeds ranged from 1 to 20 mm/s. The camera was operated at a fixed frame rate of 245 fps. Velocity fields were computed using PIVlab[22] with a multi-pass interrogation approach (64 × 64 pixels followed by 32 × 32 pixels, both with 50% overlap). For each experimental condition, a continuous video sequence was recorded. Three independently selected frame sets were analyzed using the same processing parameters, and the resulting values were averaged for quantitative analysis.

2.4. Numerical simulation

Two types of simulations were performed to characterize the filament formation during extrusion and the flow disturbance induced by needle motion, respectively. To investigate filament formation, three-dimensional simulations were performed to model the extrusion and

deposition of bioink into the supporting bath. A 23G needle was used, and the computational domain included both bioink and supporting bath phases, tracked using the volume of fluid (VOF) method. The viscosity of the bioink was defined either by a conventional power-law model or by a ML-based model capturing the coupled dependence on temperature and shear rate, also implemented via user-defined function (UDF). And the rheological behavior of the supporting bath was described by a ML model, implemented via a UDF. Mass flow rates and supporting bath velocities were varied to match experimental conditions, Although the bioink inlet temperature (22°C) and supporting bath temperature (25°C) were specified as boundary conditions, these values only define the initial thermal state of the CFD model. The simulation is fully transient, solving heat transfer and fluid flow simultaneously (Figure S3). The trained ML model was implemented via a temperature-shear-rate viscosity lookup table in ANSYS Fluent through a User-Defined Function (UDF). During each solver iteration, local temperature and shear rate are used to query the lookup table, updating local viscosity in real time. Therefore, although thermal boundaries are fixed, the viscosity field dynamically evolves throughout extrusion and deposition, capturing the filament-bath interactions. A pressure outlet was set at the exit. The nozzle wall was treated as a fixed no-slip wall. The mesh was refined near the nozzle tip and outlet (~2.9×10^6 cells). Transient simulations were performed with controlled time stepping to maintain numerical stability. The SIMPLE algorithm was used for pressure-velocity coupling, with second-order discretization schemes for pressure and momentum. Relaxation factors were set to 0.4 for pressure, 1 for density, 0.7 for momentum, and 1 for energy. Convergence criteria were set to 10^{-6} for all residuals. Grid independence was verified (Figure S4).

For the flow field analysis, two-dimensional axisymmetric simulations were conducted to represent the relative motion between the needle and the supporting bath. The needle was positioned at the center of the domain and treated as a stationary no-slip wall, while the supporting fluid was assigned uniform inlet velocities ranging from 1 to 20 mm/s. Needles with different outer diameters (21G-27G) were considered. The rheological behavior of the supporting bath was described either by a conventional HB model with experimentally determined parameters or by a ML model, implemented via a user-defined function (UDF).

The computational mesh was refined near the needle surface (~2.2×10^4 cells). The SIMPLE algorithm was used for pressure-velocity coupling, with second-order discretization schemes for pressure and momentum. Relaxation factors were set to 0.4 for pressure, 1 for density, and 0.7 for momentum. Convergence criteria were set to 10^{-6} for all residuals. Grid independence was verified (Figure S4).

2.5. Machine learning analysis

A total of 720 raw rheological measurements were collected from nine temperature groups spanning 22-30°C, with 80 measurements obtained at each temperature. Following the exclusion of the initial transient measurements at shear initiation, interquartile range (IQR)-based outlier filtering, and Savitzky-Golay smoothing of the high-temperature datasets (29-30°C). The excluded measurements corresponded to a short start-up transient period (approximately ten data points), during which the GelMA network underwent rapid structural adaptation to the applied shear field. As polymer chains and physical junctions progressively reoriented and disentangled, the apparent viscosity briefly increased before transitioning to the stable shear-thinning behavior used for subsequent analysis. Consequently, 630 valid data points were retained for model development and evaluation. To benchmark the proposed ML framework against conventional rheological approaches, a temperature-dependent Power-Law (Temp-Dep PL) model was additionally implemented, with separate Power-Law fits performed at each temperature to generate temperature-specific constitutive relationships.

The input features included temperature (°C) and shear rate (s^{-1}). To handle the wide dynamic range, both shear rate and viscosity were converted via $\log_{10}$ transformation. This transformation stabilized variance and improved regression performance. Data filtering adopted a two-step outlier removal procedure. First, values beyond the 2nd-98th percentile range were excluded. Next, data were screened against the 3 × interquartile range (IQR) threshold. For 29-30℃ tests with prominent experimental noise, a Savitzky-Golay filter with a window length of 7 and a polynomial order of 2 was used to maintain local curve consistency.

To minimize data leakage, all preprocessing steps involving data-dependent parameter estimation, including outlier threshold determination, were performed using the training set only and subsequently applied to the test set. The dataset was randomly divided into training and testing subsets at a ratio of 80:20 using a fixed random seed of 42 to ensure reproducibility. In addition, five-fold cross-validation was performed on the training set to evaluate model robustness and reduce the dependence of performance estimation on a single data partition.

The regression model was constructed as an ensemble model by combining multiple tree-based regressors. Specifically, seven Random Forest regressors and one Gradient Boosting regressor were trained independently with different random initializations. The final prediction was obtained by averaging the outputs of all individual models, thereby improving prediction stability compared with a single estimator.

This ensemble strategy was chosen because the experimental rheological dataset is moderate in size and contains measurement noise, particularly at low shear rates and near the sol-gel transition region. Tree-based methods such as Random Forests are robust to such noise and provide interpretable predictions through feature importance and ensemble averaging. Moreover, combining multiple regressors enhances model stability and predictive accuracy. Finally, the resulting ensemble model can be efficiently implemented as a lookup table within CFD simulations via UDFs, allowing integration of the learned rheology into extrusion process simulations.

For the Random Forest regressors, the number of trees was set to 300, the maximum tree depth to 30, the minimum number of samples required for splitting to 2, the minimum number of samples per leaf to 1, and the number of features considered at each split to the square root of the total number of input features. Bootstrap sampling was enabled. Each Random Forest model was trained using a different random seed to enhance ensemble diversity. The Gradient Boosting regressor was configured with 300 estimators, a maximum tree depth of 7, a learning rate of 0.05, a minimum of 2 samples per leaf, and a subsampling ratio of 0.8.

The typical operating temperature of embedded bioprinting falls around 22-25℃. To maximize prediction accuracy within this critical range, we applied a selective sample-

weighting protocol during model training. Samples in the 22-25℃ range were given higher weights, while data points outside this interval were assigned lower weights. This approach retained the full contribution of the entire dataset. This weighting scheme was used to reflect application-driven priorities in embedded bioprinting.

2.6. Data processing and error calculation

For the quantitative comparison of rheological prediction accuracy, the predictive performance of the ML and power-law models was evaluated using the mean absolute percentage error (MAPE). For each temperature-shear-rate data point, the absolute percentage error (APE) was first calculated by comparing the predicted viscosity with the corresponding experimental value. The MAPE was then obtained by averaging the APE values across the entire temperature range (22-30℃) and the full shear-rate spectrum investigated.

For the shear-rate bath disturbance analysis, the disturbance width (W) was defined as the width of the region where the shear rate exceeded 1.0 s^{-1}. For both experimental and simulation data, W was measured using the same criterion. The simulated prediction trends were obtained by linear fitting of the simulated data points. A total of 20 independent data points were included, corresponding to the combinations of 21G, 23G, 25G, and 27G nozzle diameters and printing velocities of 1, 3, 6, 12, and 20 mm s^{-1}.

For the filament morphology analysis, 12 printing conditions were designed, corresponding to three mass flow rates and four printing velocities. Among them, 10 conditions produced continuous filaments and were included in the analysis. For each printable condition, filament width (W) was measured from optical images with six independent measurements, while filament aspect ratio (W/H) was determined from three cross-sectional measurements. The experimental value for each condition was taken as the mean of the replicate measurements. The MAPE values of the ML and PL models were then calculated separately as the averages of the condition-wise APE values across the 10 experimentally characterized printing conditions.

2.7. Printing procedure

A custom-built extrusion bioprinter integrating temperature regulation, motion control, and dispensing modules was used as previously described. Digital models were created in SolidWorks or obtained from Thingiverse and processed using Cura 4.7 to generate G-code, which was further optimized using custom R scripts. Printing was conducted in a transparent acrylic chamber filled with supporting bath. A temperature-control module integrated into the x-y-z stage was used during printing. The system provided independent temperature regulation of the syringe barrel and nozzle tip over a range of 0-70℃[10]. In addition, printing was conducted within a temperature-adjustable chamber to minimize environmental temperature fluctuations. For printing, the GelMA bioink was maintained in a 37℃ water bath prior to loading into the syringe. After loading, the syringe was mounted onto the temperature-control module and equilibrated at 22℃ for 2 hours before printing. Both the syringe barrel and nozzle tip were maintained at 22℃ throughout the printing process. The H-HPMC/PF-127 supporting bath was prepared in advance and allowed to equilibrate at room temperature (25℃) for 1 hour prior to printing. Bath temperature was monitored using a K-type thermocouple. To minimize boundary effects, the printing start height was set 3 mm above the container base. Nozzles identical to those used in PIV experiments were employed, with pressures ranging from 60 to 220 kPa and translation speeds from 1 to 20 mm s^{-1}. Printed constructs were photocrosslinked using a 405 nm light source (25 mW cm^{-2}) for 1 min. Filament diameters were quantified from fluorescence images using ImageJ (n = 6 per condition). Filament states were classified based on deposition continuity and filament width. A condition was considered printable when continuous filament deposition could be maintained along the entire printing path without visible breakage. Conditions resulting in interrupted or fragmented deposition were classified as printing failures (broken filaments). Among printable conditions, filaments with widths between approximately 0.5 and 1.0 times the nozzle diameter were classified as well-defined filaments. Filaments with widths greater than the nozzle diameter were classified as over-stacked filaments, indicating excessive material accumulation during deposition. The printed models were downloaded from Thingiverse (www.thingiverse.com) (‘Hand’ by Teak

(modified), under the Creative Commons—Attribution license-CC BY 3.0—https://creativecommons.org/licenses/by/3.0/; 'DNA double helix' by Diegoso (modified), under the Creative Commons—Attribution license-CC BY 3.0—https://creativecommons.org/licenses/by/3.0/; 'Squid' by Jonoyo85 (unmodified), under the Creative Commons—Attribution license-CC BY3.0—https://creativecommons.org/licenses/by/3.0/; 'Twisted_Heart' by Gyrobot (unmodified), under the Creative Commons—Attribution license-CC BY 3.0 https://creativecommons.org/licenses/by/3.0/).'Y_junction' by chrischarlton (unmodified), under the Creative Commons—Attribution license-CC BY 3.0 https://creativecommons.org/licenses/by/3.0/).

2.8. Cell culture and bioink preparation

C2C12 myoblasts (Stem Cell Bank, cat no. SCSP-505, China) were cultured in T25 flasks under standard conditions (5% CO_2) using complete growth medium containing fetal bovine serum, antibiotics, growth factors, and basal medium (Stem Cell Bank, cat no. SCSP-M505, China). For cell-laden bioink preparation, C2C12 myoblasts were detached using 0.25% (w/v) trypsin-EDTA, collected by centrifugation (1000 rpm, 5 min), and resuspended in the 5% (w/v) GelMA with 0.5% (w/v) LAP solution at a density of 1×10^7 cells mL^{-1}. C2C12 differentiation was induced by switching to differentiation medium consisting of DMEM with 2% horse serum (Gibco #16050130) and 1% penicillin-streptomycin (Life Technologies, USA). The differentiation medium was replaced every other day, and cells were allowed to differentiate for 7 days to form myotubes.

2.9. Immunofluorescence staining and imaging

After 7 days of culture, samples were fixed with 4% paraformaldehyde (Solarbio, China), permeabilized with 0.1% Triton X-100 (Solarbio, China), and blocked with 5% bovine serum albumin (Solarbio, China). Samples were incubated overnight at 4℃ with primary antibody against Myh1 (Anti-Fast Myosin Skeletal Heavy chain Rabbit pAb, Servicebio, China, 1:100),

followed by secondary antibody staining (dylight 488 goat anti-rabbit IgG, Abbkine, China, 1:100, 1 h). Filamentous actin (F-actin) was labeled using TRITC-phalloidin (80 nM, Fushen, China), and nuclei were stained with 4', 6-diamidino-2-phenylindole (DAPI, 0.5 μg/mL, Solarbio, China). Confocal images were acquired using a Leica TCS SP8 microscope. Fluorescence intensity was quantified using ImageJ.

2.10. RNA-sequencing

Total RNA was extracted using TRIzol reagent (Invitrogen, USA) according to the manufacturer's protocol. RNA concentration and purity were assessed using a NanoDrop spectrophotometer (Thermo Scientific, USA), and integrity was evaluated prior to library preparation to ensure suitability for downstream sequencing.

For each sample, 3 μg of total RNA was used to construct sequencing libraries. Polyadenylated mRNA was isolated using oligo(dT)-attached magnetic beads and subsequently fragmented under elevated temperature in fragmentation buffer. First-strand cDNA synthesis was performed using random hexamer primers and reverse transcriptase, followed by second-strand synthesis using DNA polymerase I and RNase H. The resulting double-stranded cDNA was end-repaired, adenylated at the 3′ ends, and ligated with Illumina sequencing adapters.

Library fragments of approximately 400-500 bp were selected using AMPure XP beads (Beckman Coulter, USA) and amplified by PCR. The final libraries were quantified using an Agilent Bioanalyzer 2100 system and subjected to paired-end sequencing on the Illumina NovaSeq 6000 platform (Shanghai Personal Biotechnology Co., Ltd.).

Raw sequencing reads were processed using Fastp (v0.22.0) to remove low-quality bases, adaptor contamination, and reads with excessive unknown nucleotides, generating high-quality clean reads. The filtered reads were then aligned to the reference genome using HISAT2 (v2.1.0) with default parameters. Only uniquely mapped reads were retained for downstream analysis.

Gene-level expression quantification was performed using HTSeq (v0.9.1) to obtain raw read counts. To ensure comparability across samples, expression levels were normalized, and downstream differential expression analysis was conducted using the DESeq2 (v1.42.0) package in R, which applies a negative binomial distribution model and incorporates size-factor normalization. Differentially expressed genes (DEGs) were identified using thresholds of $|\log_2$ fold change$|$ > 1 and adjusted P value < 0.05 (Benjamini-Hochberg correction). Three independently prepared printed constructs were analyzed for each experimental group (n = 3).

To interpret the biological significance of transcriptional changes, DEGs were subjected to functional enrichment analysis using the clusterProfiler (v4.10.0) package. Gene Ontology (GO) and Kyoto Encyclopedia of Genes and Genomes (KEGG) pathway enrichment analyses were performed, and significantly enriched terms were identified based on adjusted P values. Visualization of expression patterns and enrichment results was carried out using pheatmap, enrichplot, and ggplot2.

2.11. Statistical analysis

All statistical analyses were performed using R. Data normality was assessed prior to testing. Results are presented as mean ± standard deviation. Comparisons between two groups were conducted using Student's t-test, while multiple groups were analyzed using one-way analysis of variance (ANOVA) followed by Tukey's post hoc test. The P values were provided and significance levels were as follows: * P < 0.05, ** P < 0.01, *** P < 0.001, **** P <0.0001.

3. Results

3.1. Data-driven rheology modeling for bioink and supporting bath

Because precise embedded bioprinting ultimately depends on how accurately material behavior can be described, we first established a data-driven rheology model for both the thermosensitive bioink and the supporting bath. For the GelMA bioink, rheological measurements were performed over a temperature range of 22-30 °C and a shear rate range of

0.01-100 s^{-1}. As shown in Figures 2A-B, the viscosity exhibited pronounced dependence on both temperature and shear rate. In addition to the expected shear-thinning behavior, increasing temperature caused a reduction in viscosity, indicating that the rheological response of the bioink was governed by coupled thermal and shear effects rather than by shear rate alone. The two-dimensional viscosity map and the corresponding three-dimensional viscosity landscape together provide a continuous visualization of this coupled rheological behavior.

This coupling is difficult to capture using conventional constitutive models. In particular, the power-law model requires separate fitting at each temperature, resulting in a series of discrete rheological curves that cannot provide a continuous description across the full printing condition space[18,23]. To address this limitation, we employed an ensemble learning-based regression model (ensemble model), which was selected for its ability to capture nonlinear interactions while remaining robust for relatively small experimental datasets[14]. As shown in Figure 2C, the ensemble model achieved better agreement with the experimental viscosity curves than the power-law model over the entire measured range. Quantitatively, the ensemble model reduced the overall mean absolute percentage error (MAPE) by approximately 16%. This improvement was also evident in the predicted-versus-measured comparison (Figure 2E), where ensemble predictions clustered more closely around the diagonal reference line, whereas the power-law model showed a larger spread and more systematic deviation. Importantly, the ensemble model provided a continuous viscosity landscape across both temperature and shear-rate domains, making it more suitable for process analysis under dynamically changing printing conditions.

We next applied the same data-driven strategy to the supporting bath, whose shear-dependent rheological behavior governs how the surrounding matrix responds to nozzle motion and deposited material. Compared with the conventional Herschel-Bulkley (HB) model, the ensemble model also provided more accurate fitting of the shear stress-shear rate relationship (Figure 2F). Although temperature was not explicitly considered for the supporting bath in this section, the improved fitting result indicates that the ensemble approach can more faithfully represent its effective yielding and shear-thinning behavior. Together, these results show that machine learning improves the rheological description of both the bioink and the support

material, thereby providing a more reliable basis for subsequent prediction of supporting bath disturbance and filament geometry.

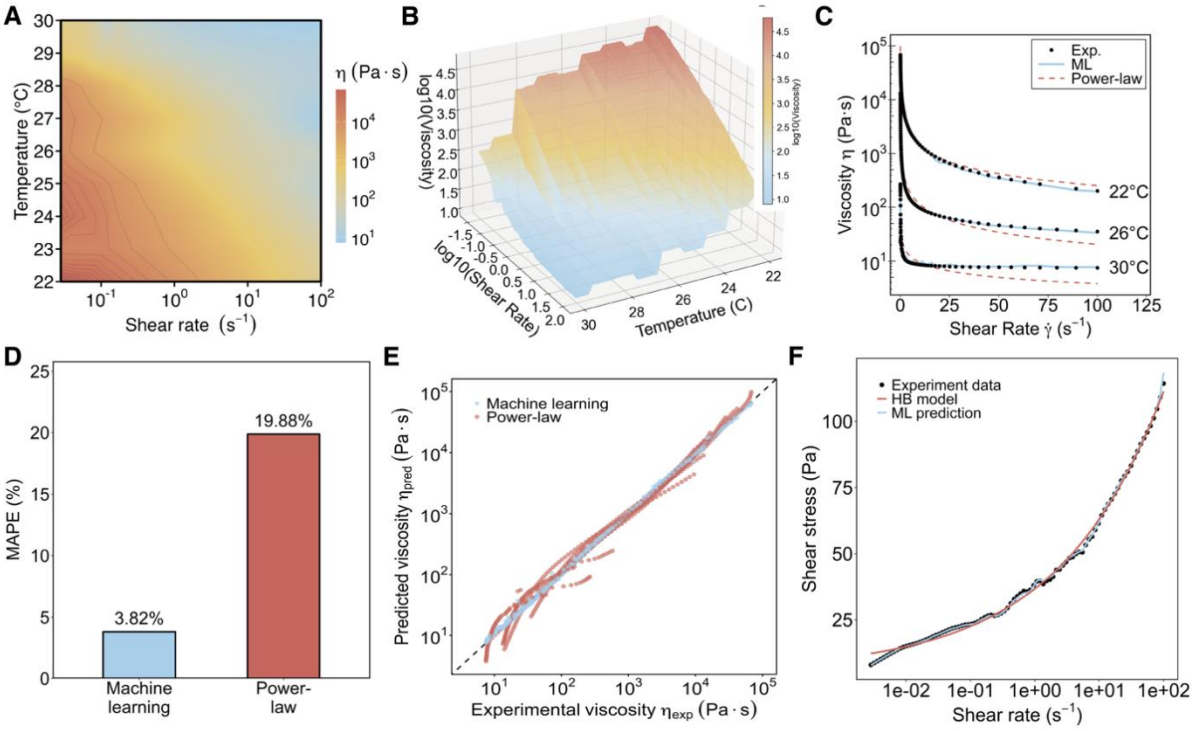

Figure 2. Data-driven modeling of bioink and supporting bath rheology. (A) Temperature-shear viscosity landscape of the thermosensitive GelMA bioink, showing the coupled dependence of viscosity on shear rate and temperature. (B) Three-dimensional viscosity landscape of the GelMA bioink across the investigated temperature and shear-rate ranges, illustrating the coupled effects of shear thinning and temperature-dependent viscosity reduction. (C) Representative viscosity-shear rate curves at several temperatures, comparing experimental measurements with predictions from the ML model and the conventional power-law model. (D) Quantitative comparison of prediction error, showing reduced MAPE for the ensemble model. (E) Predicted versus experimental viscosities, where ensemble predictions cluster more closely around the diagonal reference line than power-law predictions. (F) Shear stress-shear rate fitting of the supporting bath using ML and HB models.

3.2. Improved prediction of supporting bath disturbance

To determine whether the improved rheological description of the supporting bath can be translated into better process prediction, we next examined the flow disturbance induced by nozzle motion in the supporting bath. Before performing systematic measurements, we first compared the flow fields under extrusion ON and OFF conditions (Figures S5-S7). The velocity profiles extracted along representative horizontal and vertical directions were highly similar in the two cases, with only minor local differences near the nozzle outlet. This result indicates that the dominant disturbance in the supporting bath is mainly governed by the mechanical displacement of the moving nozzle through the viscoplastic matrix, whereas the contribution of the extruded material to the far-field flow remains limited under the tested conditions. Therefore, to avoid optical interference and boundary ambiguity caused by the printed ink, the subsequent PIV experiments were conducted under the non-extrusion condition.

Based on this simplified but representative configuration, we compared experimentally measured disturbance fields with simulations using either the conventional HB model or the machine learning (ML)-derived rheological model of the supporting bath (Figure 3A). Across different nozzle gauges and translation speeds, the experimental results consistently showed a localized disturbance zone around the moving nozzle, with strong velocity gradients near the nozzle sides and a trailing wake extending downstream. As the translation speed increased, both the intensity and spatial extent of the disturbed region increased. In contrast, reducing the nozzle diameter led to a more confined absolute disturbance zone. These trends were captured by both simulation approaches, confirming that the overall disturbance topology was primarily determined by the interaction between nozzle motion and bath rheology.

However, clear differences emerged in quantitative agreement. Compared with the HB model, the ML-based simulation more faithfully reproduced the experimentally observed width and downstream spread of the disturbed region, particularly under conditions of higher speed and smaller nozzle diameter, where the flow field became more sensitive to the rheological description. To compare different nozzle sizes and translation speeds within a unified framework[24], the disturbance width (W) was normalized by the nozzle outer diameter (d), and

the experimental conditions were further recast using an HB-derived Oldroyd number ($Od = \tau_y d^n / K U^n$, where τ_y, K, and n are the Herschel-Bulkley parameters of the supporting bath and U is the nozzle translation speed). , which served here as a common dimensionless descriptor of the operating condition rather than an intrinsic parameter of the ML model (Figure 3B). Under this representation, the normalized disturbance range (W/d) decreased approximately linearly with increasing Od (Figure 3C), indicating that the disturbance field contracted as the supporting bath became more resistant to yielding relative to nozzle motion. Notably, the ML predictions remained consistently closer to the experimental data than those of the HB model over the tested range. These results demonstrate that the data-driven rheological model provides a more accurate description of the supporting bath response to nozzle motion, thereby offering a more reliable basis for analyzing the subsequent printing process.

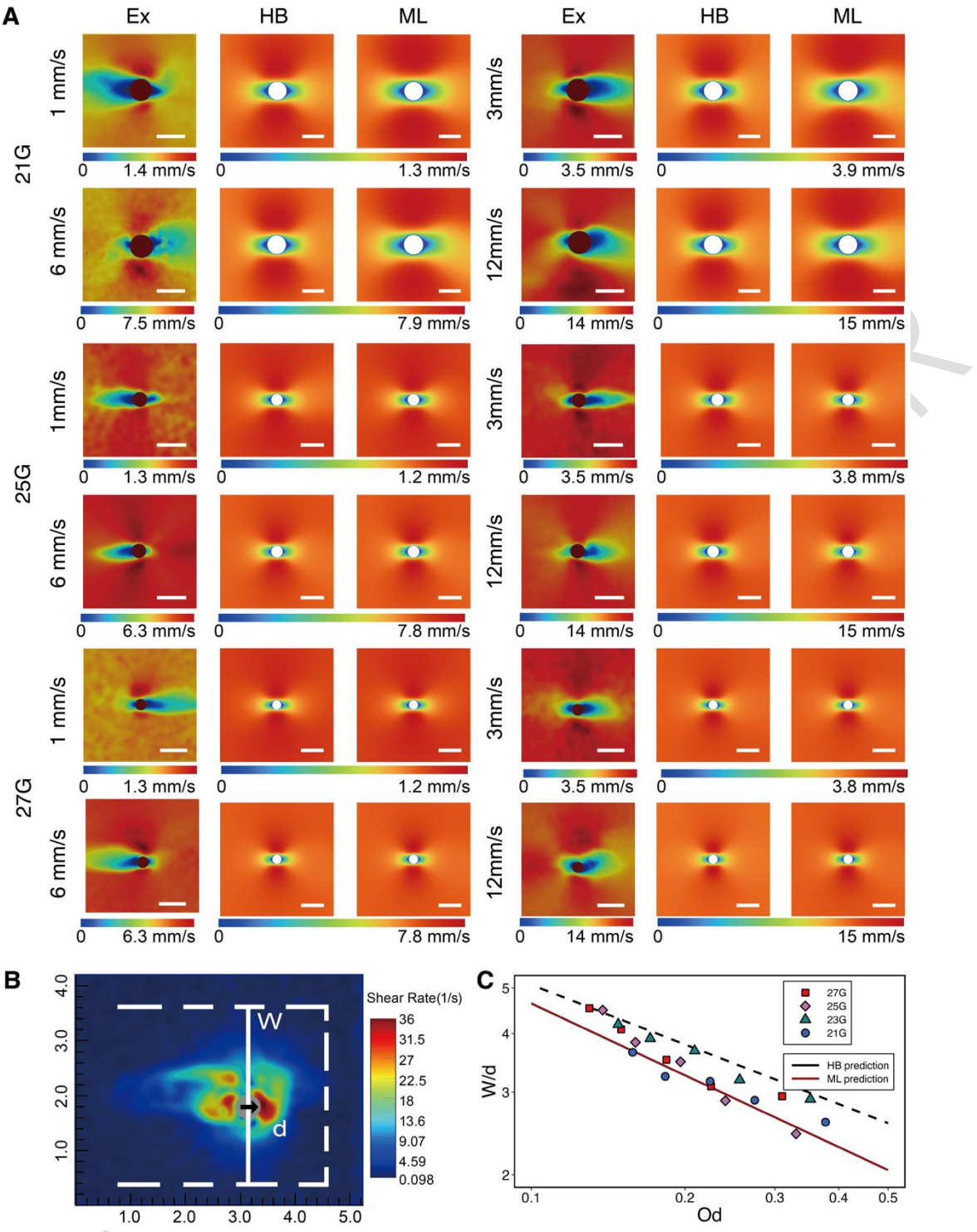

Figure 3. Prediction of supporting bath flow disturbance around the moving nozzle. (A) Comparison of experimentally measured and simulated disturbance fields around moving nozzles of different gauges and translation speeds in the supporting bath. Simulations were performed using the HB model and the ML-derived rheological model. Color maps indicate the magnitude of the local flow disturbance. Scale bars: 1 mm. (B) Definition of disturbance

width (*W*, defined as the total width of the fluid domain where the local shear rate exceeds 1.0 s^{-1}, measured uniformly across both experimental flow field images and simulation velocity data using this identical criterion) and nozzle outer diameter (*d*, defined as the actual physical outer diameter constant of the 21G, 23G, 25G, and 27G bioprinting needles, which is implemented as a fixed rigid boundary dimension in the simulation domain) used for quantitative analysis. (C) Relationship between normalized disturbance range (*W/d*, defined quantitatively as the dimensionless ratio of the extracted disturbance width *W* to the nozzle outer diameter *d* to establish a unified representation across varying nozzle sizes) and the HB-derived Oldroyd number (Od), comparing experimental measurements with HB and ML predictions. The ML model shows closer agreement with experiment across the tested conditions.

3.3. Improved prediction of filament geometry

Having established improved rheological descriptions for both the bioink and the supporting bath, we next examined whether this improvement could be translated into more accurate prediction of filament geometry during embedded printing. Since filament width, continuity, and cross-sectional shape are the most direct indicators of printing precision, accurately predicting these features is essential for moving extrusion-based bioprinting from empirical parameter tuning toward quantitative process control.

To this end, extrusion experiments were carried out under different combinations of mass flow rate (*Q*, 0.12, 0.37, and 0.51 mg/s) and translation speed (*v*, 1, 3, 5, and 7 mm/s). The extrusion process was recorded *in situ*, and the cross-sectional geometries of the deposited filaments were characterized after printing. Simulations based on either the conventional power-law model or the ML-derived rheological model were then compared with the experimental observations (Figure 4A). The experimental results showed a clear dependence of filament morphology on the balance between material supply and nozzle movement. Under low-Q/high-v conditions, the deposited filaments undergo extreme thinning and then rupture, forming discontinuous structures. Conversely, high-Q/low-v conditions lead to material

accumulation beneath the nozzle, producing broadened filaments with flattened or elliptical cross-sections. The intermediate regime between these two states yields continuous filaments with regular cross-sections. Both simulation methods capture this overall trend, and accurately reflect increasing filament width as the ratio of material throughput to nozzle velocity rises. These failure conditions define the boundary of the printable regime and therefore provide important information regarding the operational limits of embedded bioprinting. Because continuous filament formation was not achieved, filament width and cross-sectional morphology could not be reliably quantified under these conditions and were therefore excluded from subsequent geometric analyses.

However, the ML model more faithfully captured the experimentally observed transitions in filament morphology across the full parameter range. In particular, it better reproduced filament breakage under low-Q/high-v conditions and the formation of widened, elliptical cross-sections under high-Q/low-v conditions. By comparison, the power-law model tended to overestimate spreading or distortion in some cases, especially when the balance between flow rate and translation speed became unfavorable for maintaining a stable filament. These differences indicate that the coupled temperature-shear rheology embedded in the ML model is important for describing the evolving physical state of the bioink during extrusion and deposition.

To quantitatively evaluate predictive performance, filament width was plotted against $(Q/v)^{1/2}$, which provided a convenient descriptor of the balance between material delivery and nozzle motion (Figure 4B). The measured filament width increased approximately linearly with $(Q/v)^{1/2}$, consistent with the expectation that larger material input relative to translation speed produces broader deposited lines. Although both models captured this overall trend, the ML predictions followed the experimental data more closely over the full range of conditions. Further comparison of cross-sectional aspect ratio and filament width confirmed the superior performance of the ML model (Figure S8, Figure 4C). The MAPE for aspect ratio was reduced from 11.34% for the power-law model to 3.45% for the ML model, corresponding to an improvement of 7.89%. Likewise, the MAPE for filament width decreased from 10.71% to 2.73%, corresponding to an improvement of 7.98%.

Together, these results demonstrate that improving rheological prediction directly improves the predictability of filament formation in embedded printing. By more accurately capturing line breakage, cross-sectional deformation, and width scaling, the ML-based framework provides a more reliable basis for defining printable regimes and achieving controllable filament architecture.

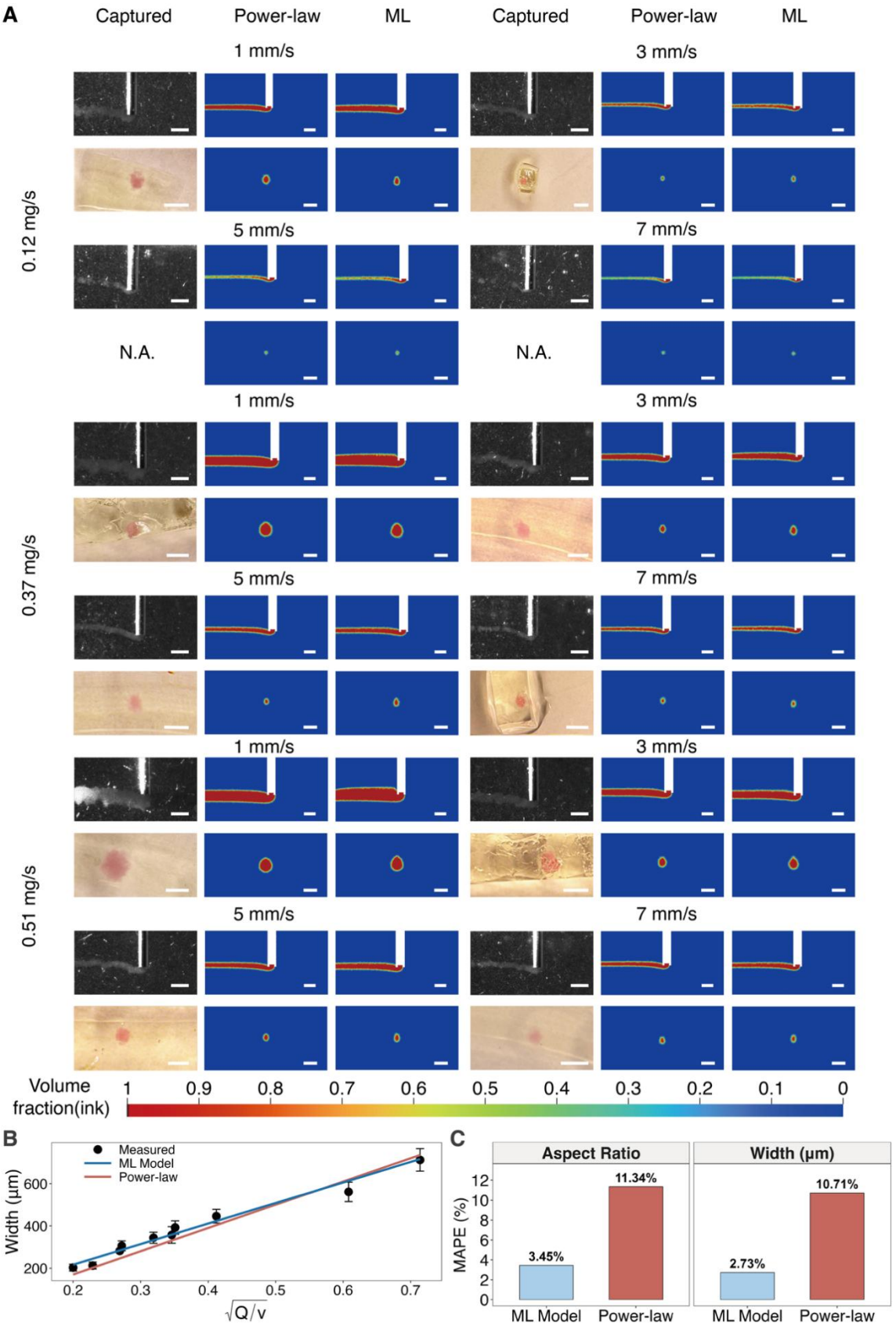

Figure 4. Improved prediction of filament geometry by machine learning-assisted rheology. (A) Experimental side-view images of extrusion and printed cross-sections under different

combinations of mass flow rate and translation speed, together with corresponding simulations based on the power-law model and the ML-derived rheological model. Scale bars: 1 mm. (B) Filament width plotted against $(Q/v)^{1/2}$, comparing measured values with predictions from the ML and power-law models (n = 3). (C) Quantitative comparison of prediction error for cross-sectional aspect ratio and filament width, showing lower MAPE (represents the average percentage error used to measure the discrepancy between experimental data and model predictions) for the ML model. N.A., conditions under which discontinuous deposition prevented reliable cross-sectional characterization.

3.4. Geometry programmability

Having established that filament formation could be predicted more accurately, we next evaluated whether this predictive capability could be translated into controllable manufacturing output. As shown in Figure 5A, the printing system enabled stable fabrication of filaments with tunable widths ranging from approximately 160 to 800 μm. As filament width increased, the deposited lines became progressively less uniform and showed more evident edge undulation, indicating stronger spreading and reduced geometric regularity at larger line widths. These results demonstrate that filament size could be programmed over a broad range while maintaining continuous deposition.

This controllable line formation further supported the fabrication of diverse freeform structures with good integrity in the supporting bath. In addition to cubic lattice architectures (Figure 5B), more complex geometries, including a Y-shaped vascular-like branch, a DNA double helix, an octopus-like model, and a hand-shaped construct, were successfully printed (Figure 5C-F). Multi-angle views confirmed that these constructs retained their intended three-dimensional shapes after deposition, indicating that the established printing conditions were sufficient to support not only line formation but also the generation of structurally complex soft constructs.

We next examined whether filament definition had early biological consequences. Live/dead staining of C2C12-laden filaments showed that viability was relatively low

immediately after printing in both groups, likely due to extrusion-associated stress (Figure 5G, H). However, viability increased progressively over the following days, suggesting gradual cellular recovery in the printed constructs. The well-defined filaments (thin and circular cross-section) showed a modestly faster recovery trend than the over-stacked (thick and oval cross-section) filaments, although the difference did not reach statistical significance. Together, these results indicate that improved control over filament geometry can be translated into programmable structure fabrication and may begin to influence the post-printing cellular microenvironment at an early stage.

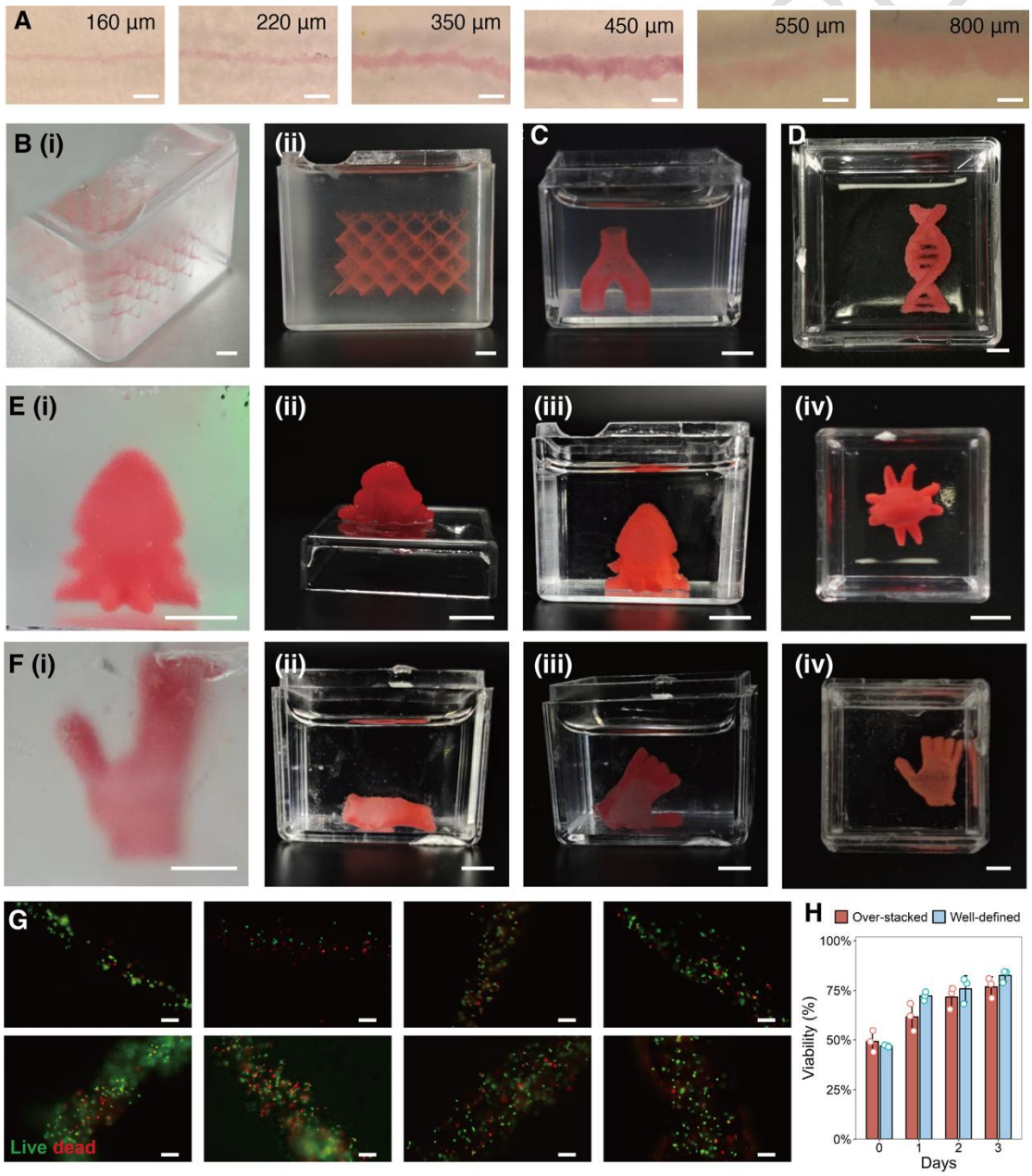

Figure 5. Geometry programmability and early cell recovery within the printable window. (A) Representative printed filaments with tunable widths from 160 to 800 μm. Scale bar: 500 μm. (B-F) Examples of freeform structures fabricated within the optimized window, including a cubic lattice, coronary artery-like construct, a DNA double helix, an octopus-like model, and a hand-shaped structure. Scale bars: 5 mm for B, C, D and F, and 10 mm for E. (G) Representative live/dead fluorescence images of cell-laden well-defined and over-stacked filaments during culture. Scale bars: 200 μm. (H) Quantification of viability over 4 days, showing progressive recovery in both groups and a faster recovery trend in the well-defined filaments (n = 3).

3.5. Biological consequences of filament definition

Having established a controllable printing window and demonstrated early differences in post-printing recovery, we next investigated whether filament definition could further influence myogenic organization and molecular state. Based on the optimized printing conditions, two architecturally distinct filament types were reproducibly generated, namely well-defined filaments with a width of approximately 125 μm and over-stacked filaments with a width of approximately 325 μm. This stable control over filament morphology provided a suitable platform for examining the relationship between filament geometry and downstream biological responses.

Confocal imaging revealed clear differences in cellular organization between the two groups (Figure 6A, B). Cells within the well-defined filaments exhibited a more aligned and elongated morphology, together with markedly stronger MHC fluorescence[25] (2.14-fold), indicating enhanced myogenic maturation compared with the over-stacked group. These observations suggest that improved filament definition may provide a structural environment that is more conducive to ordered cell arrangement and functional protein expression[3].

To determine whether these phenotypic differences were accompanied by broader molecular changes, we performed transcriptomic analysis of the two filament states. Principal component analysis (PCA) clearly separated the well-defined and over-stacked groups,

indicating that filament architecture induced a distinct global transcriptional profile (Figure 6C). The volcano plot further showed widespread differential expression, with both upregulated (108) and downregulated (164) genes contributing to the divergence between the two conditions. Pathway enrichment analysis (Table S1-S2) suggested that these changes were functionally organized rather than random. In the well-defined group, pathways related to cell adhesion molecule interactions were relatively enriched, whereas HIF-1 signaling[26], glutathione metabolism, and fluid shear stress and atherosclerosis were relatively suppressed. This pattern suggests that cells in well-defined filaments were less engaged in stress adaptation and hypoxia-associated responses[27], and instead shifted toward a more differentiation-permissive state.

The selected feature genes further supported this interpretation (Figure 6D). Acta2 was significantly increased in the well-defined group, suggesting enhanced cytoskeletal organization and contractile apparatus development[28]. Col3a1 was also upregulated, indicating strengthened extracellular matrix remodeling and structural support[29]. In parallel, the increase in Myod1 pointed to activation of the myogenic differentiation program[30]. These transcriptional changes were consistent with the elevated MHC fluorescence observed by immunostaining. By contrast, Yap1 did not show a significant difference between the two groups. Since YAP1 is a canonical mediator of mechanotransduction, its unchanged expression suggests that the observed divergence was not primarily driven by a dominant YAP-dependent mechanical signaling program at this stage[31]. Instead, when considered together with the suppression of HIF-1-related pathways and the better biological performance of the thinner filaments, the data suggest that the smaller filament dimensions may provide a more favorable microenvironment for cell survival and spreading. Previous studies have reported that, in the absence of a vascular network, the effective diffusion distance of oxygen and nutrients is typically limited to approximately 100-200 μm[32]. Since the average width of the well-defined filaments (~125 μm) was substantially smaller than that of the over-stacked filaments (~325 μm), resulting in a higher surface-area-to-volume ratio and shorter diffusion distance, differences in local oxygen and nutrient availability may contribute to the observed biological responses.

GO analysis further indicated that architectural refinement was accompanied by broader changes in cellular response programs, including transport-, secretion-, and chemotaxis-related processes. Together, these results show that printing precision has biological consequences beyond shape fidelity. The observed improvements in cell viability, spreading, and myogenic organization suggest that well-defined filaments provide a more favorable microenvironment for muscle formation. While the underlying mechanisms remain to be fully elucidated, differences in local oxygen and nutrient availability associated with filament geometry may contribute to these biological responses.

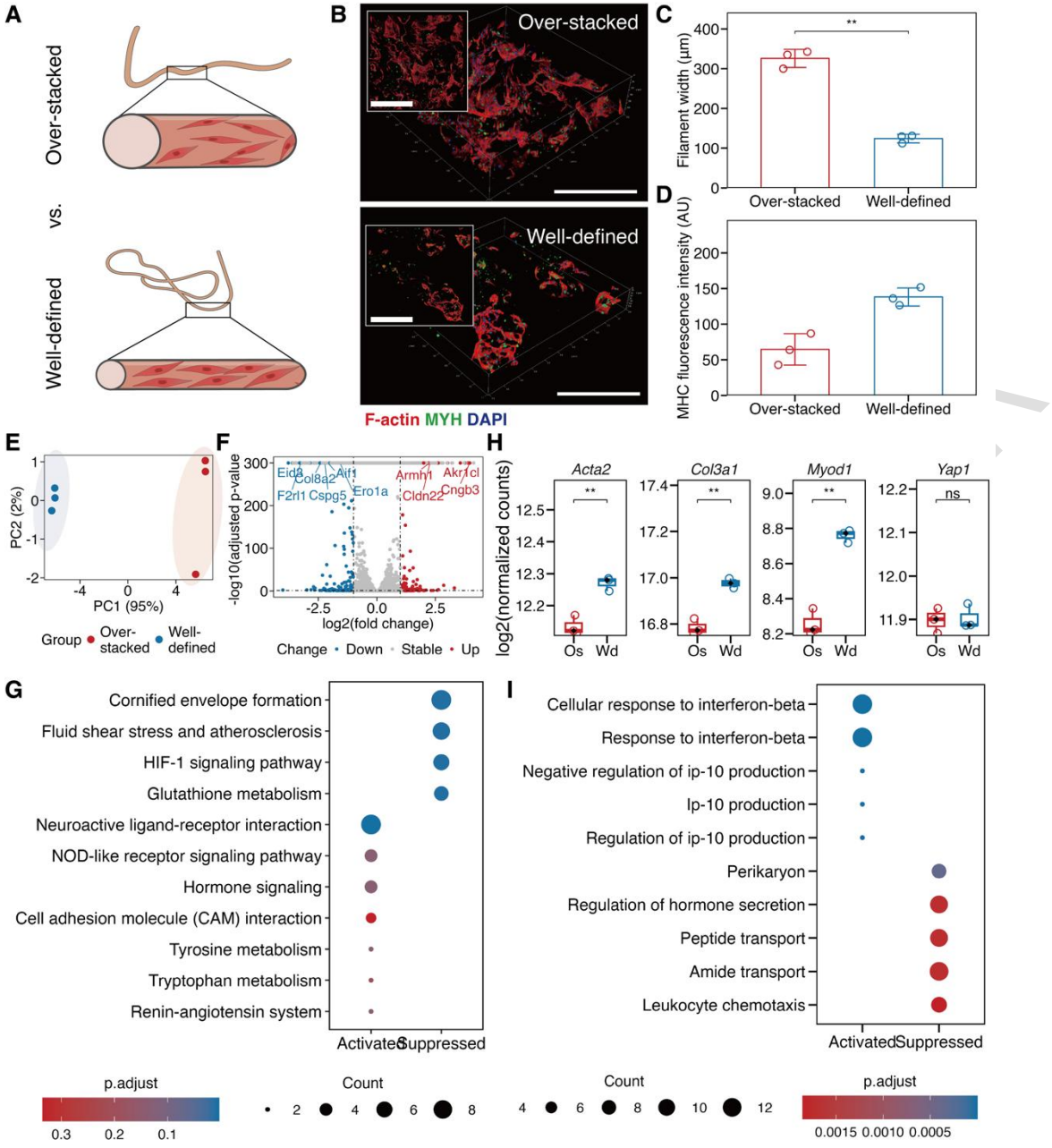

Figure 6. Biological consequences of filament definition. (A) Schematic of well-defined filament and over-stacked filaments. (B) Representative images of over-stacked and well-defined filaments after culture, showing F-actin, MHC, and nuclei staining. Scale bars: 500 μm. (C) Quantification of filament width (n = 3). (D) Quantification of MHC fluorescence intensity (n = 3). (E) PCA and (F) volcano plot showing transcriptomic divergence between over-stacked and well-defined groups. (G) KEGG enrichment analysis. (H) Expression levels of representative genes (n = 3). (I) GO enrichment analysis.

4. Discussion

This study shows that rheological accuracy has a direct impact on the predictability of embedded bioprinting. The bioink used here experiences changing shear and temperature conditions from the syringe to the nozzle and then into the supporting bath. Under these circumstances, viscosity evolves continuously during the printing process. An ensemble model was therefore well suited to this problem because it captured nonlinear coupling from experimental data without requiring a predefined equation. This provided a continuous rheological landscape for the thermosensitive GelMA bioink and improved the description of the supporting bath as well. The gain in fitting accuracy carried clear consequences for process analysis, indicating that the quality of rheological representation is a central factor in predictive printing.

The supporting bath disturbance experiments further clarified how this improved description affects nozzle-scale behavior. The close similarity between extrusion and non-extrusion disturbance fields indicates that the dominant source of far-field bath disturbance is the motion of the nozzle through the viscoplastic matrix. The contribution of the injected material is largely confined to the region near the nozzle outlet under the conditions tested here. This justified the use of non-extrusion PIV measurements and allowed the bath response to be evaluated with fewer optical and interfacial complications[24,33,34]. Within this framework, the ML-based rheological model reproduced the disturbed region more faithfully than the HB model, which suggests that it captured the effective yielding and shear-thinning response of the support matrix more accurately. Since this disturbed region governs how the matrix accommodates and stabilizes the deposited filament, the supporting bath result forms an important bridge between rheology fitting and filament formation. The proposed framework is workflow-generalizable but model-specific. The same procedure, including rheological characterization, data preprocessing, machine-learning-based rheological modeling, and CFD implementation, can be applied to other bioinks and supporting baths. The model also demonstrated reasonable robustness to reduced training-data availability (Figure S9). However, because rheological behavior is inherently material-dependent, a new dataset is required for each different material formulation, analogous to remeasuring constitutive parameters for

conventional CFD simulations. The current implementation focuses primarily on temperature–shear coupling under steady-state rheological conditions. Future extensions may incorporate time as an additional input feature to capture thixotropy, structural recovery, and other time-dependent rheological phenomena.

More importantly, this improved predictive capability was translated into controllable manufacturing output, enabling stable fabrication of filaments over a broad width range and supporting the generation of complex freeform structures with maintained integrity in the supporting bath. In this context, data-driven rheological modeling provides a practical route from process prediction to geometry programmability in embedded bioprinting.

The biological results show why this level of control matters. Filaments printed within the well-defined regime displayed a faster recovery trend after printing and later developed stronger alignment, higher MHC expression, and transcriptomic profiles associated with adhesion, matrix support, and myogenic commitment. At the same time, stress- and hypoxia-related pathways were reduced, while Yap1 remained unchanged. This pattern points to a possible microenvironmental explanation in which narrower and more regular filaments provide a more favorable structural context for cell organization. Previous studies have reported that oxygen and nutrient diffusion in avascular tissues is typically limited to approximately 100-200 μm[32]. Together with the observed improvements in cell viability, cell spreading, and HIF-1-related responses, these findings suggest that well-defined filaments may provide a more favorable microenvironment, potentially associated with improved local oxygen and nutrient availability. Future studies incorporating direct measurements of oxygen gradients, nutrient diffusion, or hypoxic responses will help further elucidate the biological mechanisms underlying the effects of filament geometry on cellular behavior. Printing precision therefore has consequences that extend into tissue maturation[35]. In this framework, filament definition becomes a biologically relevant design variable that links material behavior, process control, and functional outcome.

Although the current study focuses on the H-HPMC/PF-127 supporting bath, the proposed data-driven rheology framework is not limited to this specific system. A supporting bath that exhibits macroscopic yield stress, shear-thinning behavior, and thixotropic recovery, regardless

of its underlying microstructure, can be characterized using the same set of rheological measurements and machine learning pipeline. This may include gelatin microparticle-based baths such as FRESH, which have been demonstrated to behave as viscoplastic fluids at the macroscopic scale[36,37]. The resulting viscosity lookup table can then be integrated into CFD simulations via UDF to predict filament formation and bath disturbance.When the characteristic size of the heterogeneities, like particle diameter, is comparable to or smaller than the dominant flow length scales, such as the nozzle diameter, the continuum assumption remains valid and the framework can be applied directly. When the particle size approaches the nozzle diameter, however, the continuum assumption may no longer hold, and the filament morphology could be influenced by discrete particle rearrangements or local flow irregularities.

5. Conclusion

This study shows that improving rheological description can directly translate into predictive control in embedded bioprinting. By capturing the coupled behavior of both bioink and supporting bath using a data-driven approach, we improved the prediction of flow disturbance and filament formation, and enabled controllable fabrication across a wide geometric range. This gain in predictability was reflected at multiple levels. Filament dimensions could be programmed to support the fabrication of ultra-soft, freeform, and overhanging structures with maintained fidelity. At the same time, filament definition influenced early cellular response, with well-defined structures promoting faster recovery, improved organization, and transcriptional states consistent with enhanced myogenic progression. Taken together, these results position rheological description as a central lever in embedded bioprinting, linking material behavior to process control, structural precision, and biological outcome. This work provides a practical route toward predictive and function-oriented biofabrication.

Acknowledgments

The authors are grateful to Prof. Hongzhao Zhou and Prof. Huayong Yang for providing the laser equipment and for their insightful discussions during the preparation of this manuscript.

Funding

We would like to thank the National Natural Science Foundation of China (Grant No. 52405305) for its support.

Conflict of interest

The authors declare they have no competing interests.

Author contributions

Conceptualization: Qi Li

Formal analysis: Junyan Wang, Wenzhen Zhang, Ke Yang

Investigation: Junyan Wang, Wenzhen Zhang

Methodology: Qi Li

Visualization: Ke Yang, Bowen Zheng

Writing–original draft: Junyan Wang, Qi Li

Writing–review & editing: Qi Li

Ethics approval and consent to participate

Not applicable.

Consent for publication

Not applicable.

Availability of data

The RNA-sequencing data of C2C12 cells in bioprinted structures have been publicly deposited at GSA: CRA041774. All data used in this study are available from the corresponding author upon reasonable request

References

1. Li Q, Yu S, Wang Y, et al. Multiscale bioprinted arterial models recapitulate synergistic microenvironmental interactions in vascular disease. *Cell Biomaterials*. 2026;2(5):100257. doi:10.1016/j.celbio.2025.100257
2. Zeng Q, Yang Y, Wang H, et al. 3D printing of structural bionic and functionalized hydrogels for the construction of macroscale human cardiac tissues. *Biomaterials*. 2025;325:123573. doi:10.1016/j.biomaterials.2025.123573
3. Ding S, Ye X, Chen Y, et al. An electro-responsive functional neurovascularized engineered muscle. *Cell Biomaterials*. 2026;2(5):100305. doi:10.1016/j.cellbio.2025.100305
4. Li Q, Yu S, Wang Y, et al. Programmable embedded bioprinting for one-step manufacturing of arterial models with customized contractile and metabolic functions. *Trends Biotechnol*. 2025;43(4):918–945. doi:10.1016/j.tibtech.2024.11.019
5. Jia M, Fan T, Jia T, Liu X, Liu H, Gu Q. Temporal and spatial regulation of biomimetic vascularization in 3D-printed skeletal muscles. *Bio-Design and Manufacturing*. 2024;7(5):597–610. doi:10.1007/s42242-024-00315-0
6. Freeman S, Ramos R, Alexis Chando P, et al. A bioink blend for rotary 3D bioprinting tissue engineered small-diameter vascular constructs. *Acta Biomaterialia*. 2019;95:152 – 164. doi:10.1016/j.actbio.2019.06.052
7. Bosch-Rue E, Delgado LM, Gil FJ, Perez RA. Direct extrusion of individually encapsulated endothelial and smooth muscle cells mimicking blood vessel structures and vascular native cell alignment. *Biofabrication*. 2021;13(1):015003. doi:10.1088/1758-5090/abbd27
8. Shi L, Carstensen H, Hölzl K, et al. Dynamic Coordination Chemistry Enables Free Directional Printing of Biopolymer Hydrogel. *Chemistry of Materials*. 2017;29(14):5816 – 5823. doi:10.1021/acs.chemmater.7b00128
9. Cooke ME, Rosenzweig DH. The rheology of direct and suspended extrusion bioprinting. *APL Bioengineering*. 2021;5(1):011502. doi:10.1063/5.0031475

10. Li Q, Zhang B, Xue Q, et al. A Systematic Thermal Analysis for Accurately Predicting the Extrusion Printability of Alginate-Gelatin-Based Hydrogel Bioinks. Int J Bioprint. 2021:394. doi:10.18063/ijb.v7i3.394
11. Bhattacharjee T, Zehnder SM, Rowe KG, et al. Writing in the granular gel medium. *Science advances*. 2015;1(8):e1500655. doi:10.1126/sciadv.1500655
12. Chang H, Liu Q, Zimmerman JF, et al. Recreating the heart's helical structure-function relationship with focused rotary jet spinning. *Science*. 2022;377(6602):180 – 185. doi:10.1126/science.abl6395
13. Govindharaj M, Al Hashimi N, Soman SS, Zhou J, AlAwadhi S, Vijayavenkataraman S. 3D-bioprinted tri-layered cellulose/collagen-based drug-eluting fillers for the treatment of deep tunneling wounds. *Bio-Design and Manufacturing*. 2024;7(6):938–954. doi:10.1007/s42242-024-00305-2
14. Sarah R, Schimmelpfennig K, Rohauer R, Lewis CL, Limon SM, Habib A. Characterization and Machine Learning-Driven Property Prediction of a Novel Hybrid Hydrogel Bioink Considering Extrusion-Based 3D Bioprinting. *Gels*. 2025;11(1):45. doi:10.3390/gels11010045
15. Hu X, Wang J, Yang S, et al. Evaluation of the 3D printable temperature-responsive shape-memory PLTG terpolymers for minimally invasive surgery. *Bio-Design and Manufacturing*. 2025;8(5):709–723. doi:10.1631/bdm.2400486
16. Sun J, Gong Y, He Y, et al. Process optimization for coaxial extrusion-based bioprinting: A comprehensive analysis of material behavior, structural precision, and cell viability. *Addit Manuf*. 2025;100:104682. doi:10.1016/j.addma.2025.104682
17. Jin Y, Chai W, Huang Y. Printability study of hydrogel solution extrusion in nanoclay yield-stress bath during printing-then-gelation biofabrication. *Materials Science and Engineering: C*. 2017;80:313–325. doi:10.1016/j.msec.2017.05.144
18. Gold KA, Saha B, Rajeeva Pandian NK, et al. 3D Bioprinted Multicellular Vascular Models. *Adv Healthc Mater*. 2021;10(21):e2101141. doi:10.1002/adhm.202101141
19. He C, He J, Wu C, et al. 3D printing for tissue/organ regeneration in China. *Bio-Design and Manufacturing*. 2025;8(2):169–242. doi:10.1631/bdm.2400309
20. Oh D, Shirzad M, Chang Kim M, Chung E-J, Nam SY. Rheology-informed hierarchical machine learning model for the prediction of printing resolution in extrusion-based bioprinting. *International Journal of Bioprinting*. 2023;9(6):1280. doi:10.36922/ijb.1280
21. Li Q, Ma L, Gao Z, et al. Regulable Supporting Baths for Embedded Printing of Soft Biomaterials with Variable Stiffness. *ACS Appl Mater Interfaces*. 2022;14(37):41695–41711. doi:10.1021/acsami.2c09221
22. Thielicke W, Sonntag R. Particle Image Velocimetry for MATLAB: Accuracy and enhanced algorithms in PIVlab. *Journal of Open Research Software*. 2021;9(1):12. doi:10.5334/jors.334
23. Garcia-Cruz MR, Postma A, Frith JE, Meagher L. Printability and bio-functionality of a shear thinning methacrylated xanthan–gelatin composite bioink. *Biofabrication*. 2021;13(3):035023. doi:10.1088/1758-5090/abec2d
24. Grosskopf AK, Truby RL, Kim H, Perazzo A, Lewis JA, Stone HA. Viscoplastic Matrix Materials for Embedded 3D Printing. *ACS Applied Materials & Interfaces*. 2018;10(27):23353–23361. doi:10.1021/acsami.7b19818

25. Ding S, Li S, Shen Z, et al. Biomimetically neurovascularized engineered muscle tissue for craniofacial volumetric muscle loss. *Bio-Design and Manufacturing*. 2025;8(3):331 – 343. doi:10.1631/bdm.2400005
26. Valle-Tenney R, Rebolledo D, Acuna MJ, Brandan E. HIF-hypoxia signaling in skeletal muscle physiology and fibrosis. *J Cell Commun Signal*. 2020;14(2):147–158. doi:10.1007/s12079-020-00553-8
27. Fulco M, Cen Y, Zhao P, et al. Glucose restriction inhibits skeletal myoblast differentiation by activating SIRT1 through AMPK-mediated regulation of Nampt. *Dev Cell*. 2008;14(5):661–673. doi:10.1016/j.devcel.2008.02.004
28. Yang Y, Li L, Fei J, Li Z. C2C12 myoblasts differentiate into myofibroblasts via the TGF-beta1 signaling pathway mediated by Fibulin2. *Gene*. 2025;936:149048. doi:10.1016/j.gene.2024.149048
29. Shi A, Hillege MMG, Wust RCI, Wu G, Jaspers RT. Synergistic short-term and long-term effects of TGF-beta1 and 3 on collagen production in differentiating myoblasts. *Biochem Biophys Res Commun*. 2021;547:176–182. doi:10.1016/j.bbrc.2021.02.007
30. Shintaku J, Peterson JM, Talbert EE, et al. MyoD Regulates Skeletal Muscle Oxidative Metabolism Cooperatively with Alternative NF-kappaB. *Cell Rep*. 2016;17(2):514 – 526. doi:10.1016/j.celrep.2016.09.010
31. Judson RN, Tremblay AM, Knopp P, et al. The Hippo pathway member Yap plays a key role in influencing fate decisions in muscle satellite cells. *J Cell Sci*. 2012;125(Pt 24):6009–6019. doi:10.1242/jcs.109546
32. Takebe T, Sekine K, Enomura M, et al. Vascularized and functional human liver from an iPSC-derived organ bud transplant. Nature. 2013:481–484. doi:10.1038/nature12271
33. Shin S, Kwak H, Shin D, Hyun J. Solid matrix-assisted printing for three-dimensional structuring of a viscoelastic medium surface. *Nature Communications*. 2019;10(1):4650. doi:10.1038/s41467-019-12585-9
34. Zhao J, Hussain M, Wang M, Li Z, He N. Embedded 3D printing of multi-internal surfaces of hydrogels. *Additive Manufacturing*. 2020;32:101097. doi:10.1016/j.addma.2020.101097
35. Wang Z, Wang X, Huang Y, et al. Cav3. 3-mediated endochondral ossification in a three-dimensional bioprinted GelMA hydrogel. *Bio-Design and Manufacturing*. 2024;7(6):983–999. doi:10.1007/s42242-024-00287-1
36. Hinton TJ, Jallerat Q, Palchesko RN, et al. Three-dimensional printing of complex biological structures by freeform reversible embedding of suspended hydrogels. *Science advances*. 2015;1(9):e1500758. doi:10.1126/sciadv.1500758
37. Lee A, Hudson A, Shiwarski D, et al. 3D bioprinting of collagen to rebuild components of the human heart. *Science*. 2019;365(6452):482–487. doi:10.1126/science.aav9051